

See discussions, stats, and author profiles for this publication at: <https://www.researchgate.net/publication/231513783>

# Mechanistic Insights into the Crystallization of Amorphous Calcium Carbonate (ACC)

ARTICLE in CRYSTAL GROWTH & DESIGN · JULY 2012

Impact Factor: 4.89 · DOI: 10.1021/cg300676b

CITATIONS

57

READS

154

5 AUTHORS, INCLUDING:



[Juan Diego Rodriguez-Blanco](#)

University of Copenhagen

42 PUBLICATIONS 543 CITATIONS

SEE PROFILE



[Teresa Roncal-Herrero](#)

The University of York

17 PUBLICATIONS 241 CITATIONS

SEE PROFILE



[Sam Shaw](#)

The University of Manchester

99 PUBLICATIONS 988 CITATIONS

SEE PROFILE



[Liane G Benning](#)

Helmholtz-Zentrum Potsdam - Deutsches Geo...

132 PUBLICATIONS 2,872 CITATIONS

SEE PROFILE

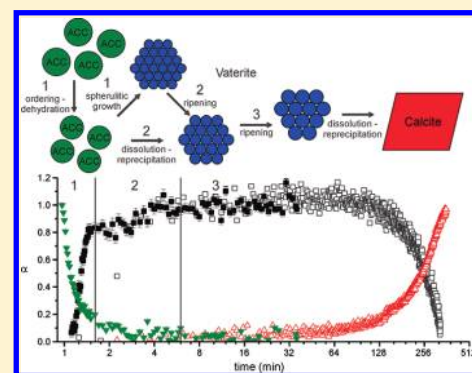
# Mechanistic Insights into the Crystallization of Amorphous Calcium Carbonate (ACC)

Pieter Bots,<sup>†</sup> Liane G. Benning, Juan-Diego Rodriguez-Blanco, Teresa Roncal-Herrero, and Samuel Shaw\*

Earth Surface Science Institute, School of Earth and Environment, University of Leeds, Leeds LS2 9JT, U.K.

## Supporting Information

**ABSTRACT:** Many organisms use amorphous calcium carbonate (ACC) during crystalline calcium carbonate biomineralization, as a means to control particle shape/size and phase stability. Here, we present an in situ small- and wide-angle X-ray scattering (SAXS/WAXS) study of the mechanisms and kinetics of ACC crystallization at rapid time scales (seconds). Combined with offline solid and solution characterization, we show that ACC crystallizes to vaterite via a three-stage process. First, hydrated and disordered ACC forms, then rapidly transforms to more ordered and dehydrated ACC; in conjunction with this, vaterite forms via a spherulitic growth mechanism. Second, when the supersaturation of the solution with respect to vaterite decreases sufficiently, the mechanism changes to ACC dissolution and vaterite crystal growth. The third stage is controlled by Ostwald ripening of the vaterite particles. Combining this information with previous studies, allowed us to develop a mechanistic understanding of the abiotic crystallization process from ACC to vaterite and all the way to calcite. We propose this is the underlying abiotic mechanism for calcium carbonate biomineralization from ACC. This process is then augmented or altered by organisms (e.g., using organic compounds) to form intricate biominerals. This study also highlights the applicability of in situ time-resolved SAXS/WAXS to study rapid crystallization reactions.



## INTRODUCTION

The anhydrous crystalline calcium carbonate ( $\text{CaCO}_3$ ) polymorphs, which form under ambient conditions, are calcite, aragonite, and vaterite. Their crystallization in both abiotic and biotic systems is often preceded by the formation and subsequent transformation of amorphous calcium carbonate (ACC). Synthetic calcium carbonates with specific particle sizes, shapes, and structures can be produced using the ACC formation pathway. Large quantities are manufactured for many industrial applications (e.g., paper manufacture and pharmaceuticals); however, in some cases, their precipitation is highly undesirable (e.g., scale formation in oil pipes), which leads to high repair/replacement costs. Calcium carbonates also form in a wide variety of natural environments (e.g., soils and sediments) and are ubiquitous at the Earth's surface. For example, calcium carbonate is the major component of ancient limestone deposits or modern marine reefs. Most modern, natural calcium carbonate phases are formed by organisms as biominerals, which fulfill a wide variety of functions (e.g., stability and protection). The most common and stable calcareous biominerals are calcite and aragonite.<sup>1</sup> However, in some cases, less stable vaterite is biomineralized<sup>1b</sup> (e.g., in spicules of an ascidian<sup>2</sup> and various fish otoliths<sup>3</sup>). Despite their importance, a clear understanding of the fundamental processes controlling the crystallization of calcium carbonate is still lacking.

Many biomineralizing organisms utilize the ACC pathway to precisely control the particle shape and crystalline polymorph<sup>1a</sup>

during the formation of their shells or spines etc.<sup>4</sup> For example, sea urchin larvae produce highly elongated single crystals of calcite by the controlled deposition and transformation of ACC within a biological membrane.<sup>5</sup> Such natural biological processes have informed biomimetic studies of crystal growth and design and are now used to manipulate the shape and size of synthetic calcium carbonate particles.<sup>6</sup>

The structure and chemistry of ACC is complex with several forms of ACC classified according to their water content, local order, and mode of formation (e.g., abiotic vs biogenic).<sup>7</sup> A key variable is the amount of structural water. Hydrated-ACC can contain up to  $\sim 1.6$  mol of water per mole of  $\text{CaCO}_3$ , yet several less hydrated and even anhydrous forms of ACC have been described. For example, Radha et al.<sup>7b</sup> produced both disordered and less disordered ACC with different degrees of hydration. Observations by Politi et al.<sup>5</sup> during sea urchin spicule formation showed that initially hydrated ACC forms, which transformed to anhydrous ACC before crystallizing to calcite via a secondary nucleation process. The enthalpies of the ACC phases in relation to the crystalline calcium carbonates show that energetically the sequence of increasing stability and possible crystallization pathway<sup>8</sup> is as follows: disordered, hydrated ACC  $\rightarrow$  less disordered, less hydrated ACC  $\rightarrow$  anhydrous ACC  $\rightarrow$  vaterite  $\rightarrow$  aragonite  $\rightarrow$  calcite.<sup>7b</sup> This sequence highlights that all ACC phases have higher formation

Received: May 17, 2012

Published: May 21, 2012



enthalpies than the crystalline polymorphs; thus, ACC can act as a precursor to any of the anhydrous crystalline phases. However, in inorganic systems, the transformation of ACC to its crystalline counterparts is often extremely rapid (seconds to minutes),<sup>9</sup> and because of their inherent instability, the ACC precursors are difficult to characterize using *ex situ* techniques (e.g., TEM and FTIR). Therefore the proposed sequence of polymorph formation has not yet been observed in full or quantified in detail.

Abiotically synthesized ACC rapidly transforms to vaterite, calcite, or aragonite, with the polymorph formed dependent on a number of factors including time, fluid composition, presence of organic molecules, and temperature.<sup>10</sup> In most cases, pure ACC will transform to calcite via a vaterite intermediate at low temperatures (<30 °C)<sup>9,10c</sup> and to aragonite via vaterite at higher temperatures (>60 °C).<sup>10c</sup> At low temperatures, the addition of magnesium tends to favor the direct formation of calcite from ACC, without a vaterite intermediate.<sup>10b</sup> In contrast, sulfate has been shown to increase the stability and persistence of vaterite significantly at low temperatures and may be key to understanding the stabilization of vaterite in biological and environmental systems.<sup>11</sup>

The mechanisms and kinetics of the later stages of the crystallization pathways have been shown to be controlled by the dissolution of vaterite and precipitation of calcite, with the rate controlled by the surface area of calcite.<sup>9,12</sup> However, the mechanism of the ACC to vaterite transformation is still not clear, with several possible mechanisms proposed. Many studies have suggested that ACC dissolves and vaterite spheres formed via homogeneous nucleation of nanocrystalline vaterite particles, followed by fast aggregation to form micrometer sized polycrystalline spheres.<sup>13</sup> A solid state mechanism for the ACC to vaterite crystallization has also been proposed, with the ACC particles dehydrating and recrystallizing to form vaterite.<sup>9,14</sup> Finally, a recent study, based on imaging of inorganically precipitated vaterite, suggested that vaterite forms via ACC dissolution coupled to spherulitic growth.<sup>15</sup> Resolving the mechanisms and kinetics of ACC crystallization in abiotic systems is key to developing a detailed understanding of how calcium carbonate phases form in both natural and synthetic processes. In particular, the mechanism of transformation between the individual phases forming as the system moves toward thermodynamic equilibrium from disordered hydrated ACC to fully crystalline calcite needs to be fully quantified. However, it should be noted that many biomineralization processes occur entirely within a biological membrane with little or no free water and in the presence of organic macromolecules.<sup>1a</sup> Therefore, any abiotic mechanism of ACC crystallization in solution may be altered or manipulated by the organism during biomineral formation.

In this study, we performed *in situ* small- and wide-angle X-ray scattering (SAXS/WAXS) experiments with a time resolution of 1 s to study the direct transformation of ACC to vaterite in solution and the effect of sulfate on this reaction. Combined with offline characterization of the solid phases and solution composition, we show that the crystallization of ACC to vaterite occurs in three distinct stages. First, the initial ACC phase dehydrates and vaterite forms via rapid spherulitic growth. This is followed by an intermediate stage where vaterite continues to form from the dissolving ACC, and finally, the vaterite particle grows via surface-controlled Ostwald ripening. In addition, the presence of sulfate decreased the overall

crystallization rate and reduced the particle growth rate during Ostwald ripening.

## ■ MATERIALS AND METHODS

**Crystallization Experiments.** The crystallization of pure ACC (without additive) was performed both offline and online, using the same method and experimental setup, by rapidly mixing equal volumes of molar solutions of calcium chloride (1 M, CaCl<sub>2</sub>·2H<sub>2</sub>O, >99% purity) and sodium carbonate (1 M, Na<sub>2</sub>CO<sub>3</sub>, >99% purity). These pure ACC experiments were complemented with sets of experiments performed with either 10 mol % of the Na<sub>2</sub>CO<sub>3</sub> replaced by Na<sub>2</sub>SO<sub>4</sub> (SO<sub>4(repl)</sub> experiments) as sulfate is thought to replace carbonate in some calcium carbonate phases<sup>18</sup> and with 10 mol % Na<sub>2</sub>SO<sub>4</sub> added to the Na<sub>2</sub>CO<sub>3</sub> solution (SO<sub>4(add)</sub> experiments) to determine the effects of sulfate as a true additive. During mixing and throughout the whole experimental time, the suspensions were vigorously stirred to ensure rapid and continual homogenization. The composition, solution volumes, and saturation indices with respect to vaterite ( $SI = \log[a_{Ca^{2+}}a_{CO_3^{2-}}/K_{sp,vaterite}]$ , where  $a$  denotes the activity of the ion in the subscript) of the starting solutions used for all experiments are listed in Table S1 (Supporting Information).

**Offline Data Collection and Analyses.** During all offline experiments, the pH was continuously recorded (5–10 s time steps), and aliquots of the suspensions and solutions were removed at regular intervals and filtered using 0.2 μm membrane filters. The solids were immediately washed with isopropanol and dried.<sup>16</sup> The solution samples were analyzed by ion chromatography (IC) for Ca and SO<sub>4</sub>.<sup>11a</sup> Together with the pH, the measured concentrations were used to calculate the aqueous carbonate concentration/speciation and the saturation index (SI) with respect to vaterite over the whole length of the experiments using PHREEQC, with the activity coefficients calculated using the Davis equation.<sup>17</sup> The solid powders were imaged with a Field Emission Gun Scanning Electron Microscope (LEO 1530 Gemini FEG-SEM), and the particle size distributions of ACC and vaterite were determined by measuring the diameters of ~100 particles.

**Synchrotron SAXS/WAXS Data Collection.** The online, *in situ* experiments were performed using the simultaneous SAXS/WAXS data collection capability of beamline I22 at Diamond Light Source, U.K. Immediately after mixing, the suspensions were continuously pumped via a peristaltic pump through a capillary in line with the synchrotron beam. Simultaneous 2D SAXS (collected with a RAPID detector)<sup>18</sup> and 1D WAXS (collected with a HOTWAXS detector)<sup>19</sup> patterns ( $\lambda = 1\text{Å}$ ) were collected at one second time frames for the total reaction duration of ~35 min. SAXS patterns were only collected for the pure ACC and SO<sub>4(repl)</sub> experiments. Because of practical beamline operating procedures, data collection started ~60 s after mixing.

**SAXS/WAXS Data Processing.** All SAXS and WAXS patterns were detector response corrected and background subtracted using a scattering pattern from the Na<sub>2</sub>CO<sub>3</sub>/Na<sub>2</sub>SO<sub>4</sub> solution. Individual WAXS patterns were fitted using Topas 4.2<sup>20</sup> to obtain the Rietveld scale factor ( $S$ ) for vaterite. The Rietveld scale factor relates the structure of a crystalline phase to the area under the Bragg peaks to obtain the amount of the respective phase in the sample.<sup>21</sup> Normalizing the Rietveld scale factor from the WAXS patterns throughout the experiments ( $S(t)$ ) to the Rietveld scale factor at the end of the experiment ( $S_{\text{final}}$ ) gives the degree of reaction for vaterite ( $\alpha_{\text{vaterite}} = S(t)/S_{\text{final}}$ ).<sup>9</sup> Similarly, the background intensity ( $B(t)$ ) from the WAXS pattern normalized to the background intensity at  $t = 0$  ( $B_0$ ) and the end of the experiment ( $B_{\text{final}}$ ) was used to calculate the degree of reaction for the ACC breakdown ( $\alpha_{\text{ACC}} = (B(t) - B_{\text{final}})/(B_0 - B_{\text{final}})$ ).<sup>9</sup> Finally, selected SAXS patterns were analyzed with GNOM<sup>22</sup> to obtain information about the ACC particle size, while the change in vaterite crystallite size was determined from the scattering peak position in the SAXS patterns using  $d = 2\pi/q$ , where  $d$  (nm) is particle diameter and  $q$  (nm<sup>-1</sup>) is the scattering vector.<sup>23</sup>



## RESULTS

**SAXS/WAXS.** In all experiments, upon mixing, a white gel-like precipitate formed instantaneously. Offline XRD showed that this initial precipitate was ACC, confirming previous analysis of material synthesized using the same method.<sup>9</sup> At the start of data collection ( $\sim 60$  s after mixing), no Bragg peaks were observed in the WAXS patterns, only a broad hump caused by scattering from the ACC and aqueous solution (Figure 1A). With time, the background intensity decreased,

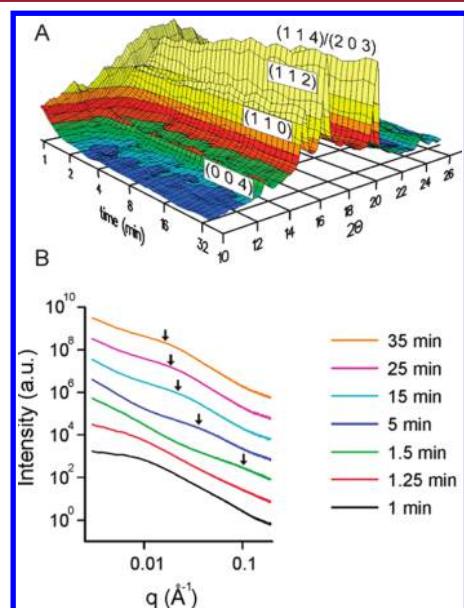


**Figure 1.** (A) Three-dimensional representations of the time-resolved WAXS patterns from the pure ACC experiment (time is plotted on a base 2 log scale for clarity); (B) stacked time series of selected SAXS patterns from the pure ACC experiment, with the legend showing time in minutes and the arrows illustrating the position of the peaks caused by the scattering from the growing vaterite crystallites.

due to the ordering/dehydration of the ACC<sup>7b</sup> and/or ACC transformation. Following this, the growth of Bragg peaks was observed (Figures 1A and S1, Supporting Information). All Bragg peaks could be assigned to vaterite, and no other crystalline phases were observed throughout the length of all experiments (max. 35 min). The time series SAXS patterns (Figure 1B) showed that simultaneous with the appearance of the Bragg peaks in the WAXS patterns (at  $\sim 1.5$  min, Figure 1A), a peak in the SAXS patterns appeared (Figure 1B). Over time, this peak migrated to lower  $q$ , indicating particle growth.

**Reaction Pathway.** The degree of reaction ( $\alpha$ ) for the crystallization of vaterite from pure ACC was extracted from the WAXS patterns (Figure 1A) as described above. Combining  $\alpha_{\text{ACC}}$  and  $\alpha_{\text{vaterite}}$  with the pH evolution from an equivalent offline experiment revealed that the transformation occurred in three distinct stages (Figure 2A). The first stage was characterized by a rapid decrease in  $\alpha_{\text{ACC}}$  up to  $\sim 80$  s, with a concomitant rapid increase in  $\alpha_{\text{vaterite}}$  between  $\sim 70$  and  $\sim 90$  s (Figure 2A). At the end of this first stage,  $\alpha_{\text{vaterite}}$  and  $\alpha_{\text{ACC}}$  were  $\sim 0.8$  and  $\sim 0.2$ , respectively (Figure 2A). During the second stage of the reaction,  $\alpha_{\text{ACC}}$  decreased to zero after  $\sim 4$ – $6$  min, and vaterite continued to form but at a slower rate reaching a plateau after  $\sim 6$  min. Finally, during the third stage, the  $\alpha_{\text{vaterite}}$  remained constant, indicating that the crystallization from ACC was complete. The corresponding pH profile revealed a fast

decrease from  $\sim 9.6$  to  $\sim 8.3$  during the first two stages of the reaction (Figure 2A) and subsequent stabilization during stage three. Data for the crystallization of vaterite in the presence of sulfate (Figures 2B and S2, Supporting Information,  $\text{SO}_{4(\text{add})}$  and  $\text{SO}_{4(\text{repl})}$ ) followed an equivalent 3-stage reaction, with the initial formation of vaterite delayed by  $\sim 40\%$  in the  $\text{SO}_{4(\text{add})}$  experiment.

The particle diameters for vaterite and ACC, evaluated from the SAXS data, are plotted in Figure 2C,D. The results reveal that in the early part of stage one ( $< 70$  s), when vaterite was not yet present, ACC particles with diameters of  $\sim 35$ – $40$  nm formed in both the pure ACC and  $\text{SO}_{4(\text{repl})}$  experiments (Figure 2D). These values are comparable with the particle sizes evaluated from the FEG-SEM images ( $42 \pm 14$  nm; Figure 3A). There is a slight increase in ACC particle size with time during stage 1; however, the majority of ACC formed prior to the start of the SAXS/WAXS data collection ( $< 60$  s). The first vaterite particles that formed during stage one ( $\sim 70$  s) had initial diameters of  $\sim 9$  nm (Figure 2C) in both experiments (pure ACC and  $\text{SO}_{4(\text{repl})}$ ). During stage two ( $90$  s to  $6$  min), the vaterite particle size increased rapidly to  $\sim 35$  nm in the pure ACC system and to  $\sim 20$  nm in the  $\text{SO}_{4(\text{repl})}$  system (Figure 2C). Finally, during stage three, although the  $\alpha_{\text{vaterite}}$  remained constant (Figure 2A), the particle size continued to increase reaching a final diameter of  $\sim 60$  nm in the pure ACC system and  $\sim 40$  nm in  $\text{SO}_{4(\text{repl})}$  system (Figure 2C). The appearance and persistence of scattering peaks in the SAXS patterns indicate that the vaterite crystallite sizes are relatively monodisperse throughout the experiments.<sup>23,24</sup> FEG-SEM observation of solids collected during stage two (at 2 min) showed the vaterite as large ( $1.3 \pm 0.4$   $\mu\text{m}$ ) polycrystalline spheres consisting of much smaller individual vaterite crystallites of  $\sim 34 \pm 7$  nm in size (Figure 3B), yet some remnant ACC was still present in the samples. Finally, images of the sample from the end of stage three (at 35 min) showed similar large polycrystalline spheres (Figure 3C) but consisting of crystallites of  $58 \pm 16$  nm (Figure 2C) without any remnant ACC. Comparing the vaterite particle sizes from the SAXS and SEM analysis indicates that the SAXS patterns recorded the size of the individual crystallites rather than the micrometer sized polycrystalline spheres. Additional analyses of the SAXS patterns from the pure ACC experiment in terms of the time evolution of the Porod slope ( $p$ , see also Supporting Information)<sup>25</sup> showed a decrease in  $p$  during stage one from  $\sim 3.4$  to  $\sim 2.5$  and a gradual increase during stage three to  $\sim 2.9$  (Figure S3, Supporting Information).

**Solution Chemistry.** The aqueous calcium concentrations measured immediately after mixing showed that  $\sim 80$ – $95\%$  of the initial calcium (500 mM, Table S1, Supporting Information) was removed from solution during the precipitation of ACC ( $< 60$  s; Figure 4A). During stage two, the calcium concentrations reached a constant value, which was maintained for the whole duration of the experiments (Figure 4A). Comparing the three different experiments shows that the calcium concentrations were significantly higher throughout the  $\text{SO}_{4(\text{repl})}$  experiment ( $\sim 75$ – $50$  mM) compared to the pure ACC and  $\text{SO}_{4(\text{add})}$  experiments ( $\sim 30$ – $10$  mM). This was due to an excess in calcium relative to carbonate in the starting solution (Table S1, Supporting Information). The evolution of the sulfate concentrations was similar in both the  $\text{SO}_{4(\text{add})}$  and  $\text{SO}_{4(\text{repl})}$  experiments (Figure 4B). In stage one, the sulfate concentrations decreased by 20–30% compared to the initial

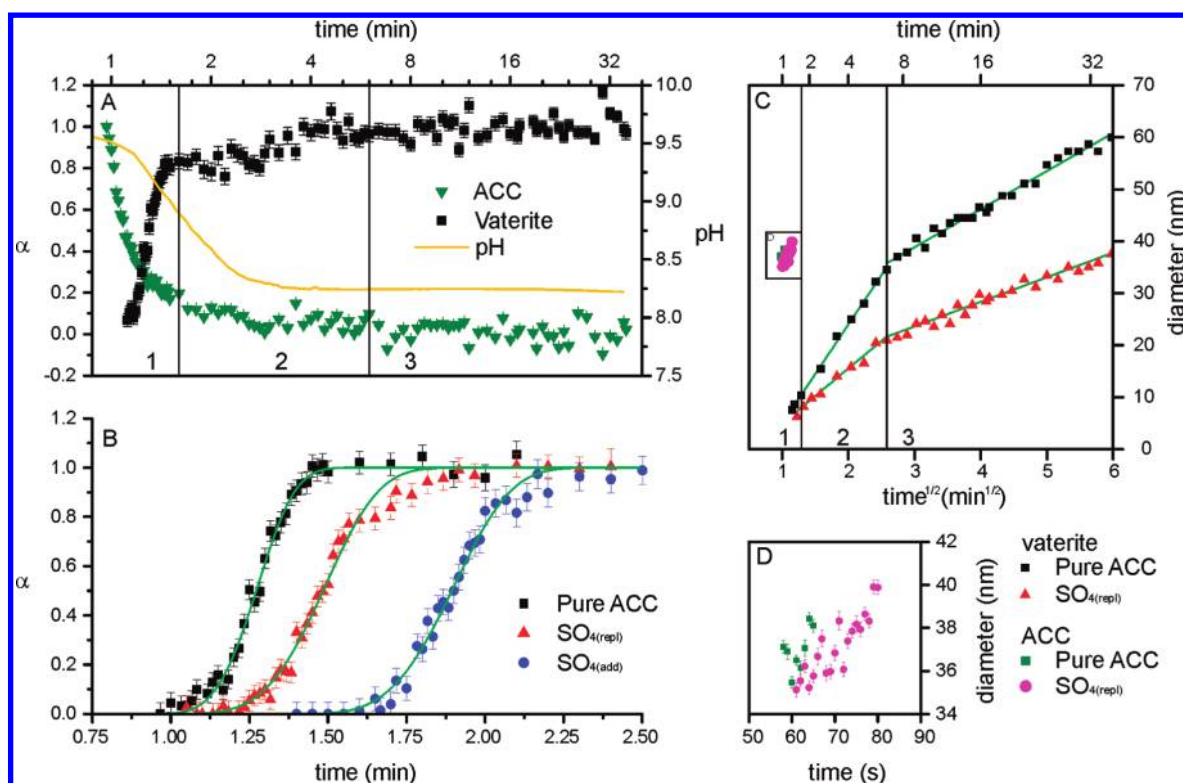


**Figure 2.** (A)  $\alpha_{\text{vaterite}}$  ( $\alpha_{\text{vaterite}} = (S(t)/S_{\text{final}})$ ,  $\alpha_{\text{ACC}}$  ( $\alpha_{\text{ACC}} = (B(t) - B_{\text{final}})/(B_0 - B_{\text{final}})$ ), and pH vs time (base 2 log scale) plot for the ACC to vaterite transformation in the pure ACC experiment. (B)  $\alpha_{\text{vaterite}}$  vs time plots for the 1st stage of the crystallization of vaterite for all experiments with the best fit lines (see below) in green. Pure ACC refers to the system with no sulfate;  $\text{SO}_4(\text{repl})$  refers to the systems with sulfate replacing 10% of the carbonate; and  $\text{SO}_4(\text{add})$  refers to the system where 10% sulfate was added to the carbonate solution. (C) ACC nanoparticle and vaterite crystallite sizes derived from the SAXS data vs time (on a  $t^{1/2}$  scale) for the pure ACC and  $\text{SO}_4(\text{repl})$  experiments. (D) ACC nanoparticle size vs time corresponding to the inset in panel C; vertical lines and numbers at the bottom of panels A and C represent the three stages of the reaction.

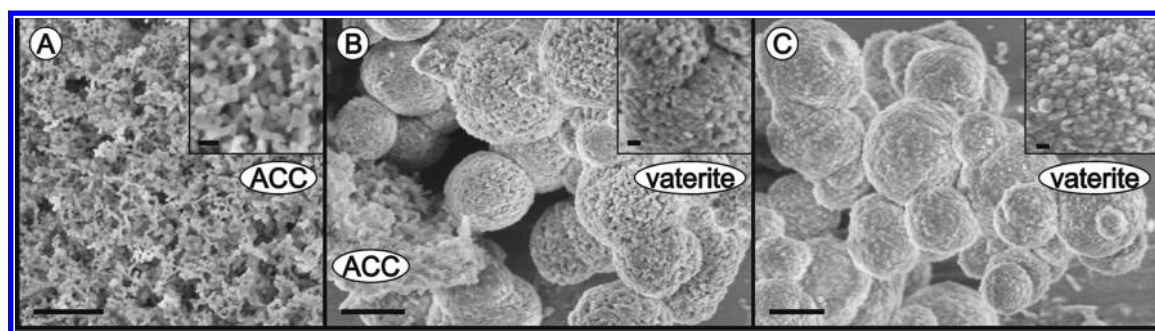


**Figure 3.** FEG-SEM images of solids quenched throughout the pure ACC experiment; (A) 1 min, (B) 2 min, and (C) 35 min. The scale bar is 1  $\mu\text{m}$  in the main images; the insets are enlargements of the dominant phase ((A) ACC and (B,C) vaterite) in their respective main images, and the scale bar in the insets is 100 nm.

values (50 mM, Table S1, Supporting Information) and reached relatively constant values through stages two and three.

## DISCUSSION

**Stage One: ACC Formation and Vaterite Spherulitic Growth.** Immediately upon mixing of the initial solutions, ACC precipitated with particle sizes (35–40 nm; Figure 2D) consistent with a previous study where ACC was synthesized using the same synthesis protocol (20–45 nm).<sup>9</sup> This is in contrast to other studies that have reported ACC with larger particle diameters, e.g., 90–110 nm,<sup>26</sup> ~270 nm,<sup>27</sup> and ~125 nm.<sup>16</sup> However, in these previous studies, ACC was precipitated from solutions of significantly lower supersaturation ( $\text{SI} = 1.7\text{--}2.3$ ;  $[\text{Ca}]$  and  $[\text{CO}_3] = 3.5\text{--}10$  mM after

mixing) compared to the initial supersaturation in this study ( $\text{SI} = 4.2$ ; Table S1, Supporting Information). As the number of nuclei increases with supersaturation<sup>28</sup> and the amount of reactant in the system is finite, the final particles size of ACC will decrease with increasing supersaturation.<sup>29</sup>

The rapid decrease in WAXS background intensity before the formation of vaterite (<70 s, Figures 1A and S1, Supporting Information) in conjunction with a decrease in the concentration of dissolved calcium (Figure 4A) suggests that the structure and/or composition of the ACC phase in our experiments changes during this first stage of the reaction. The decrease in the WAXS background cannot be due to dissolution of the ACC, as this would lead to an increase in  $[\text{Ca}^{2+}]$  and pH, both of which are not observed. Recent thermodynamic<sup>7b</sup> and

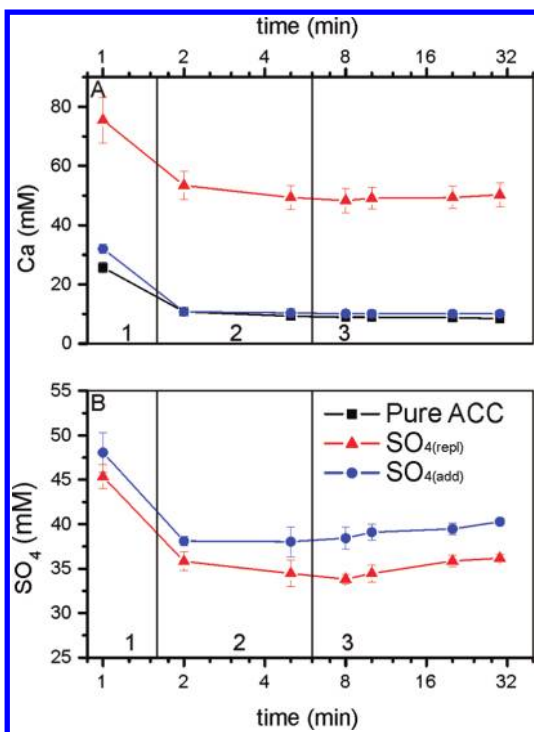


**Figure 4.** Evolution of the solution composition with time (base 2 log scale); (A) calcium and (B) sulfate; the black vertical lines and numbers in both figures indicate the different reaction stages, and the errors bars represent the standard deviation of three measurements.

spectroscopic studies<sup>5,30</sup> of the crystallization of ACC in abiotic and biotic systems have shown that freshly precipitated, hydrated ACC transforms to a more stable (lower enthalpy) dehydrated ACC prior to crystallization. This more thermodynamically stable form of ACC is also somewhat more structurally ordered compared to the less stable and more hydrated initial ACC phase.<sup>7b</sup> The observed decrease in WAXS background intensity in the current study is also indicative of an increase in local order and dehydration of the initial ACC.<sup>9</sup> We suggest that the dehydration/ordering process was driven by lowering the enthalpy of the ACC.<sup>7b</sup> This is also supported by the decrease in pH and  $\text{Ca}^{2+}$  concentration (Figures 2A and 4A), during the early stages of the reaction (prior to vaterite formation), which could be caused by the formation of the lower solubility dehydrated/ordered ACC, leading to a lowering of the overall carbonate concentration in solution and reduced pH. Therefore, the first step in the transformation of ACC to vaterite was the dehydration and ordering of ACC, which occurred before significant crystallization of vaterite was observed.<sup>7b,31</sup>

The transformation of ACC to vaterite as observed here must allow for a very rapid crystallization rate. In the pure ACC system, it only took  $\sim 20\text{--}30$  s to reach  $\alpha_{\text{vaterite}} \approx 0.8$  at the end of stage one (Figure 2A). Primarily on the basis of electron microscopic observations, three possible mechanisms for the ACC to vaterite crystallization have so far been proposed: (i) homogeneous vaterite nucleation followed by fast aggregation,<sup>13</sup> (ii) solid-state transformation to vaterite,<sup>9,14</sup> and (iii) fast spherulitic growth of vaterite polycrystalline spheres.<sup>15</sup> Pouget et al. observed the solid-state transformation of ACC to vaterite in the presence of a template and of dissolved ammonium,<sup>14</sup> which stabilized the (001) planes of vaterite and leads to large hexagonal plate-like vaterite particles, unlike the

polycrystalline spheres in this study. Therefore, this solid-state mechanism is not directly comparable to results in the current study. In contrast, spherulitic growth has been shown to occur via growth front nucleation (GFN),<sup>32</sup> where new particles grow via the continuous nucleation of misaligned equivalent structural units (crystallites) on the surface of a growing spherulite.<sup>33</sup> Such a growth mechanism tends to result in polycrystalline spheres consisting of crystallites of approximately equal sizes. This is consistent with the vaterite morphology observed in the FEG-SEM images (Figure 3B), with micrometer sized spheres consisting of nanometer sized crystallites (Figure 2C). Additionally, the diameter of the vaterite crystallites that formed at the end of stage one ( $\sim 9$  nm) was similar to the  $\sim 10$  nm  $\varnothing$  for the crystallites in spherulitically grown vaterite as reported by Andreassen.<sup>15</sup> In order for continuous nucleation to be the dominant growth process during spherulitic growth, the solution has to be continuously highly supersaturated with respect to the crystallizing phase. Andreassen<sup>15</sup> suggested that the spontaneous nucleation of vaterite, and therefore spherulitic growth, will always occur in the presence of ACC due to the large difference in solubility between these two phases (i.e.,  $K_{\text{sp,ACC}} = 10^{-6.3}$  and  $K_{\text{sp,vaterite}} = 10^{-7.74}$ ).<sup>34</sup> Nucleation of vaterite in the presence of ACC forces the highly soluble ACC to dissolve and maintain a high supersaturation ( $\text{SI} = 1.6$ , which is equivalent to a saturation ratio  $\sigma = 5$  where  $\sigma = (a_{\text{Ca}^{2+}}a_{\text{CO}_3^{2-}}/K_{\text{sp,vaterite}})^{1/2} - 1$ <sup>15</sup>) with respect to vaterite. The saturation index of the solution with respect to vaterite is high during stage one ( $\text{SI} > 1.4/\sigma = 5$ ; Figure 5 and Table S2, Supporting Information) but

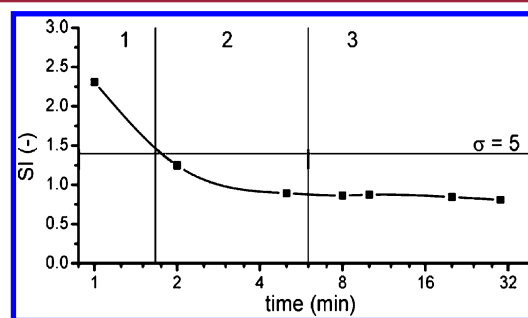


**Figure 5.** Evolution of the saturation indices vs time (base 2 log scale) for the pure ACC system (based on PHREEQC calculations, further summarized in Table S2, Supporting Information); the vertical lines separate the three stages of the transformation reaction; the SI for the initial solution (prior to ACC precipitation) is not plotted, which was  $\sim 4.2$  (Table S1, Supporting Information). The horizontal line shows the supersaturation ratio ( $\sigma$ ) of 5.<sup>15</sup>

reduces to approximately 1 at the end of this stage. We suggest that the high supersaturation during stage one allows vaterite to form via spherulitic growth supporting the growth mechanism of Andreassen.<sup>15</sup> Gránásy et al.<sup>32</sup> used theoretical calculations to determine that, during spherulitic growth, the extent of crystallization follows a Johnson–Mehl–Avrami–Kolmogorov (JMAK) kinetic model of the form:

$$\alpha(t) = \exp[1 - k(t - t_0)^n]$$

where  $k$  is the kinetic constant ( $\text{min}^{-n}$ ),  $t$  is the time (min),  $t_0$  is the induction time (min), and  $n$  is the Avrami exponent. The Avrami exponent can be expressed as  $n = d + 1$ ,<sup>32</sup> where  $d$  is the dimensionality during spherulitic growth. The images in Figure 3 show that the vaterite spherulites have grown in three



dimensions; therefore, an Avrami exponent of 4 would be expected (Figure 2B and Table S3, Supporting Information). This model fits very well to the growth of vaterite during stage one ( $R^2 > 0.98$ ; Table S3, Supporting Information), which further strengthens our hypothesis that vaterite formed via a spherulitic growth mechanism. This growth mechanism contradicts the solid-state mechanism proposed in our previous study.<sup>9</sup> Our current opinion is that the solid-state transformation does not occur and that vaterite forms by the spherulitic mechanism described above.

In addition, the Porod slope from the SAXS plots from the pure ACC experiments ( $p$ , Supporting Information) is  $\sim 3.4$  after 1 min (Figure S3, Supporting Information), indicating the presence of particles with rough surfaces (i.e., surface fractal).<sup>24,25b</sup> After 2 min,  $p$  decreased to  $\sim 2.5$  (Figure S3, Supporting Information), which corresponds to mass fractal particles.<sup>35</sup> This change in  $p$  corresponds with the transformation from ACC particles ( $\varnothing \sim 35$  nm, Figure 2D) with rough surfaces to the polycrystalline aggregates of vaterite particles with mass fractal characteristics (i.e., micrometer sized polycrystalline spheres consisting of  $\sim 9$  nm crystallites, Figure 3B).

**Effect of Sulfate on Vaterite Spherulitic Growth.** A significant decrease in the crystallization rate constant during stage two in both sulfate systems compared to the pure ACC system was calculated using the JMAK model (pure ACC,  $k = 48.7 \pm 8.8 \text{ min}^{-4}$ ;  $\text{SO}_{4(\text{repl})}$ ,  $k = 11.7 \pm 2.5 \text{ min}^{-4}$ ;  $\text{SO}_{4(\text{add})}$ ,  $k = 9.2 \pm 2.3 \text{ min}^{-4}$ ; Table S3, Supporting Information). This could either be caused by sulfate decreasing vaterite nucleation by surface interactions or by sulfate changing the bulk stability (i.e., enthalpy/lattice energy) of vaterite. Recent studies showed that sulfate stabilizes vaterite (i.e., decrease lattice energy)<sup>11</sup> and that it has no significant influence on the stability of ACC,<sup>36</sup> thus potentially increasing the reaction enthalpy for the ACC–vaterite transformation. This suggests that the observed decrease in rate constant (Table S3, Supporting Information) was not a result of bulk thermodynamic changes caused by the presence of sulfate. It is more likely that this decrease was due to adsorption of sulfate, which poisoned nucleation sites on the growing vaterite spherulites and thus decreased the rate of GFN. A similar effect has been observed during calcite growth, with sulfate poisoning calcite growth sites.<sup>37</sup>

In our experiments, the start of vaterite spherulitic growth was only delayed in the  $\text{SO}_{4(\text{add})}$  system (Figures 2B and S2, Supporting Information). However, the start of vaterite spherulitic growth in the  $\text{SO}_{4(\text{repl})}$  system was not significantly delayed despite sulfate being present. This indicates that the differences in induction time cannot be explained solely by the presence of sulfate. The calcium (Figure 4A) and calculated total inorganic carbon and bicarbonate concentrations (Table S2, Supporting Information) were larger in the  $\text{SO}_{4(\text{repl})}$  compared to the  $\text{SO}_{4(\text{add})}$  system during stage one. In addition, there is no significant difference in the SI with respect to vaterite between the  $\text{SO}_{4(\text{repl})}$  and  $\text{SO}_{4(\text{add})}$  systems (Table S2, Supporting Information). We suggest that bicarbonate had a destabilizing effect on ACC, as previously suggested by Nebel et al.,<sup>38</sup> therefore, the inhibiting effect of sulfate on vaterite formation was counteracted by the presence of high bicarbonate concentrations accelerating ACC breakdown. Also, it has previously been observed for calcite growth that the growth rate depends on the concentration of bicarbonate rather than carbonate.<sup>39</sup> Therefore, the reduction in the induction time (Table S3, Supporting Information) in the

$\text{SO}_{4(\text{repl})}$  may also be due to the higher bicarbonate concentration.

### Stages Two and Three: Vaterite Growth and Ripening.

The vaterite crystallized during stage two ( $\sim 20\%$  of total; Figures 2A and S2, Supporting Information) formed under near equilibrium saturation conditions (Figure 5). During this stage, virtually no increase in the vaterite spherulite size was observed (Figure 3B,C), thus excluding further spherulitic growth. Furthermore, the calcium concentration in solution (Figure 4A) decreased only slightly, indicating that little additional calcium carbonate precipitated from solution. At the end of stage one,  $\alpha_{\text{ACC}} \approx 0.2$  (Figure 2A) and  $\alpha_{\text{vaterite}} \approx 0.8$ ; therefore, we suggest that the final 20% of vaterite formed by the dissolution of the remaining ACC and reprecipitation on the pre-existing vaterite crystallites that nucleated during stage one. The lowered vaterite SI during stage two ( $< 1.2$ ; Figure 5 and Table S2, Supporting Information) also suggests that the solubility of the remaining ACC was significantly reduced. We argue that this was caused by the ordering/dehydration of ACC, which would lower the ACC enthalpy and solubility.<sup>7b</sup>

In stage two, the crystallite size of the vaterite particles making up the large spherulites increased from  $\sim 9$  nm to  $\sim 37$  nm (Figure 2C). Assuming that this increase was only caused by 3D spherical growth via ACC dissolution, this would indicate a 70 times increase in the total mass of vaterite. However, because the WAXS analyses showed that only  $\sim 20\%$  of the total vaterite formed during stage two, we conclude that an alternative mechanism must be responsible for the majority of the increase in vaterite crystallite size. We suggest that this process is Ostwald ripening.<sup>40</sup> Ostwald ripening can either occur by a diffusion or surface controlled mechanism. When Ostwald ripening is diffusion controlled,  $r(t) \propto t^{1/3}$  (where  $r(t)$  is particle radius (nm) and  $t$  is time (seconds)); and when Ostwald ripening is surface/reaction controlled,  $r(t) \propto t^{1/2}$ . As the solutions were stirred continuously during the experiments (i.e., the suspensions were kept homogeneous), control of the reaction via diffusion through the fluid can be eliminated, and the Ostwald ripening process was likely to be surface controlled. This was also confirmed by the linearity of the plot of  $d$  versus  $t^{1/2}$  (Figure 2C).

Finally, the vaterite particle growth in stage three was purely controlled by Ostwald ripening as no additional vaterite formed after stage two. Again, the linearity of the plot of  $d$  versus  $t^{1/2}$  (Figure 2C) suggests a continued surface controlled ripening reaction. During stage three, the Porod slope ( $p$ ) also increased from 2.5 to 2.9 (Figure S3, Supporting Information). This was caused by a decrease in fractal appearance of the vaterite spherulites<sup>35</sup> as the crystallites increase in size due to Ostwald ripening (see also Supporting Information).

### Effect of Sulfate on Vaterite Growth and Ripening.

The final particle size of the vaterite crystallites was  $\sim 40\%$  smaller in the  $\text{SO}_{4(\text{repl})}$  compared to the pure ACC system (Figure 2C), which suggests that sulfate is reducing the rate of ripening, probably via adsorption onto the growing particles. The particle growth rate during Ostwald ripening is controlled by a number of factors including surface free energy and bulk solubility.<sup>40</sup> The surface free energy of calcium carbonates can be changed by the adsorption of dissolved ions.<sup>41</sup> Such a decrease in the surface free energy for vaterite was observed in the presence of silica,<sup>42</sup> and we assert that sulfate may have a similar effect on the surface free energy of the growing vaterite crystallites. Additionally, incorporation of sulfate into vaterite decreases its lattice energy<sup>11b</sup> and increases its stability.<sup>11</sup>

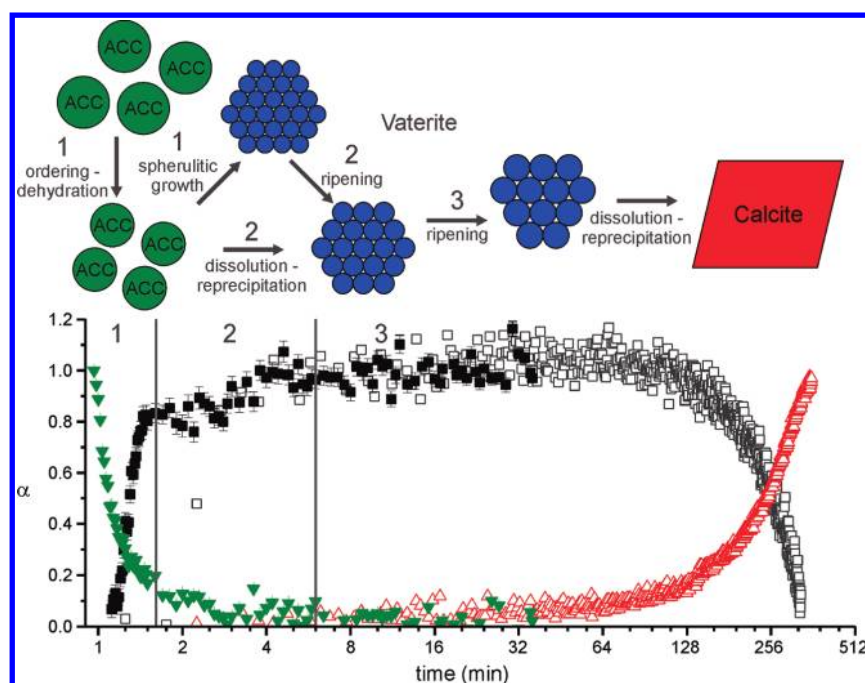


**Figure 6.** Schematic representation of the proposed multistage ACC  $\rightarrow$  vaterite  $\rightarrow$  calcite crystallization pathway (top) with the underlying combined reaction progress,  $\alpha_{\text{ACC}}$ ,  $\alpha_{\text{vaterite}}$ , and  $\alpha_{\text{calcite}}$  for the full crystallization reaction in the pure ACC system (the green triangles and full black squares represent the ACC and vaterite from this study, and the open squares and red triangles represent the vaterite and calcite from Rodriguez-Blanco et al.<sup>9</sup>); stages 1, 2, and 3 of the reaction mechanism are labeled on the figure.

Hence, the bulk solubility of vaterite may decrease in the presence of sulfate, which would also decrease the ripen rate.

## SUMMARY AND CONCLUSIONS

Combining the mechanisms presented above with previous results on the transformation of vaterite to calcite<sup>9,12</sup> allowed us to elucidate the full abiotic transformation pathway from ACC via vaterite to calcite (Figure 6). In the first stage, disordered hydrated ACC forms from a highly supersaturated solution. The local order within the ACC then increases concurrent with dehydration. This transition occurs due to the lower enthalpy of the more ordered less hydrated phase.<sup>7b</sup> The large difference in solubility between ACC and vaterite in stage one keeps the supersaturation at a sufficiently high level to allow continuous vaterite nucleation and spherulitic growth.<sup>15</sup> Once initiated, spherulitic growth is maintained as long as highly soluble ACC is present in the system. The ordering and increase in thermodynamic stability (lower enthalpy) of the ACC is also confirmed by a observed transition from spherulitic vaterite growth to surface particle growth in stage two, which indicates that the solubility of the ACC decreased. Once all of the ACC has been consumed, the vaterite crystallite size continues to increase via Ostwald ripening (stage two and three). Because Ostwald ripening is a dissolution reprecipitation mechanism,<sup>40</sup> the further ripening of the vaterite is easily displaced by a dissolution–reprecipitation transformation mechanism leading to the final calcite.<sup>9,12</sup> This multistep reaction pathway validates the relative stability scheme for the various amorphous and crystalline calcium carbonate phases as described by Radha et al.<sup>7b</sup>

The reaction pathway described above provides a comprehensive description of the abiotic mechanism of pure ACC crystallization. This multistage reaction process may represent the pathway of pure ACC biomineralization. This is supported

by the observation of Killian et al.<sup>30</sup> who showed that calcitic sea urchin spicules form by secondary calcite nucleation within the ACC. This matches the secondary nucleation of vaterite then calcite in the abiotic reaction sequence. This shows that, in both systems, the solubility difference between ACC and calcite/vaterite is large enough to allow continuous homogeneous nucleation of the crystalline phases from a solution in equilibrium with ACC. We propose that the abiotic mechanism described above is the underlying fundamental pathway of ACC crystallization. During biomineralization, organisms may adjust, tailor, or control this process using organic molecules or membrane structures to form the exact phase and shape required. For example, many biomineralized calcium carbonates contain magnesium, which leads to the direct crystallization of calcite.

This study also shows that sulfate reduces the rate of vaterite formation and particle growth but has no large mechanistic influence on ACC crystallization. However, sulfate has the capability to stabilize vaterite and may be intrinsic to stabilizing biomineralized vaterite.<sup>1b,2,3,11</sup> Finally, the results presented in this study demonstrate how fast time-resolved SAXS/WAXS data can be obtained and evaluated to gain an unprecedented understanding into fast crystallization reactions when combined with offline solid and solution characterization.

## ASSOCIATED CONTENT

### Supporting Information

Solution chemistry data of the initial solutions from the experiments; additional WAXS and SAXS analyses; and modeling results (from the PRHEEQC program and the JMAK model). This material is available free of charge via the Internet at <http://pubs.acs.org>.



## AUTHOR INFORMATION

### Corresponding Author

\*E-mail: s.shaw@see.leeds.ac.uk.

### Present Address

<sup>†</sup>Research Centre for Radwaste and Decommissioning, The University of Manchester, Manchester M13 9PL, U.K.

### Author Contributions

The manuscript was written through contributions of all authors. All authors have given approval to the final version of the manuscript.

### Notes

The authors declare no competing financial interest.

## ACKNOWLEDGMENTS

We would like to acknowledge the European Union Marie-Curie Research and Training Network "Mineral Nucleation and Growth Kinetics (MIN-GRO)" for funding (grant MRTNCT-2006-035488) and Diamond Light Source (grant no 57701 to L.G.B.) for beamtime at the SAXS/WAXS beamline (I22) for the in situ and time-resolved experimental work. Finally, we would like to acknowledge Dr. Mike Krom and Dr. Caroline Peacock for their useful comments on the manuscript.

## REFERENCES

- (1) (a) Weiner, S.; Dove, P. M. An Overview of Biomineralization Processes and the Problem of the Vital Effect. In *Biomineralization*; Dove, P. M., de Yoreo, J. J., Weiner, S., Eds.; Mineralogical Society of America: Washington, DC, 2003; Vol. 54, pp 1–29. (b) Lowenstam, H. A. Minerals Formed by Organisms. *Science* **1981**, *211* (4487), 1126–1131.
- (2) Lowenstam, H. A.; Abbott, D. P. Vaterite: A Mineralization Product of the Hard Tissues of a Marine Organism (Ascidacea). *Science* **1975**, *188* (4186), 363–365.
- (3) Tomás, J.; Geffen, A. J. Morphometry and Composition of Aragonite and Vaterite Otoliths of Deformed Laboratory Reared Juvenile Herring from Two Populations. *J. Fish Biol.* **2003**, *63* (6), 1383–1401.
- (4) (a) Weiss, I. M.; Tuross, N.; Addadi, L.; Weiner, S. Mollusc Larval Shell Formation: Amorphous Calcium Carbonate Is a Precursor Phase for Aragonite. *J. Exp. Zool.* **2002**, *293* (5), 478–491. (b) Politi, Y.; Arad, T.; Klein, E.; Weiner, S.; Addadi, L. Sea Urchin Spine Calcite Forms via a Transient Amorphous Calcium Carbonate Phase. *Science* **2004**, *306* (5699), 1161–1164.
- (5) Politi, Y.; Metzler, R. A.; Abrecht, M.; Gilbert, B.; Wilt, F. H.; Sagi, I.; Addadi, L.; Weiner, S.; Gilbert, P. U. P. A. Transformation Mechanism of Amorphous Calcium Carbonate into Calcite in the Sea Urchin Larval Spicule. *Proc. Natl. Acad. Sci. U.S.A.* **2008**, *105* (50), 20045–20045.
- (6) (a) Meldrum, F. C.; Cölfen, H. Controlling Mineral Morphologies and Structures in Biological and Synthetic Systems. *Chem. Rev.* **2008**, *108* (11), 4332–4432. (b) Gower, L. B. Biomimetic Model Systems for Investigating the Amorphous Precursor Pathway and Its Role in Biomineralization. *Chem. Rev.* **2008**, *108* (11), 4551–4627.
- (7) (a) Gebauer, D.; Gunawidjaja, P. N.; Ko, J. Y. P.; Bacsik, Z.; Aziz, B.; Liu, L.; Hu, Y.; Bergström, L.; Tai, C.-W.; Sham, T.-K.; Edén, M.; Hedin, N. Proto-Calcite and Proto-Vaterite in Amorphous Calcium Carbonates. *Angew. Chem., Int. Ed.* **2010**, *49* (47), 8889–8891. (b) Radha, A. V.; Forbes, T. Z.; Killian, C. E.; Gilbert, P. U. P. A.; Navrotsky, A. Transformation and Crystallization Energetics of Synthetic and Biogenic Amorphous Calcium Carbonate. *Proc. Natl. Acad. Sci. U.S.A.* **2010**, *107* (38), 16438–16443.
- (8) Van Santen, R. A. The Ostwald Step Rule. *J. Phys. Chem.* **1984**, *88* (24), 5768–5769.
- (9) Rodriguez-Blanco, J. D.; Shaw, S.; Benning, L. G. The Kinetics and Mechanisms of Amorphous Calcium Carbonate (ACC) Crystallization to Calcite, via Vaterite. *Nanoscale* **2011**, *3* (1), 265–271.
- (10) (a) Lam, R. S. K.; Charnock, J. M.; Lennie, A.; Meldrum, F. C. Synthesis-Dependant Structural Variations in Amorphous Calcium Carbonate. *CrystEngComm* **2007**, *9* (12), 1226–1236. (b) Rodriguez-Blanco, J. D.; Bots, P.; Roncal-Herrero, T.; Shaw, S.; Benning, L. G. The Role of pH and Mg on the Stability and Crystallization of Amorphous Calcium Carbonate. *J. Alloys Compd.* **2012**, in press. (c) Ogino, T.; Suzuki, T.; Sawada, K. The Formation and Transformation Mechanism of Calcium Carbonate in Water. *Geochim. Cosmochim. Acta* **1987**, *51* (10), 2757–2767.
- (11) (a) Bots, P.; Benning, L. G.; Rickaby, R. E. M.; Shaw, S. The Role of SO<sub>4</sub> in the Switch from Calcite to Aragonite Seas. *Geology* **2011**, *39* (4), 331–334. (b) Fernández-Díaz, L.; Fernández-González, Á.; Prieto, M. The Role of Sulfate Groups in Controlling CaCO<sub>3</sub> Polymorphism. *Geochim. Cosmochim. Acta* **2010**, *74* (21), 6064–6076.
- (12) Ogino, T.; Suzuki, T.; Sawada, K. The Rate and Mechanism of Polymorphic Transformation of Calcium Carbonate in Water. *J. Cryst. Growth* **1990**, *100* (1–2), 159–167.
- (13) (a) Vacassy, R.; Lemaître, J.; Hofmann, H.; Gerlings, J. H. Calcium Carbonate Precipitation Using New Segmented Flow Tubular Reactor. *AIChE J.* **2000**, *46* (6), 1241–1252. (b) Stávek, J.; Šípek, M.; Hirasawa, I.; Toyokura, K. Controlled Double-Jet Precipitation of Sparingly Soluble Salts. A Method for the Preparation of High Added Value Materials. *Chem. Mater.* **1992**, *4* (3), 545–555. (c) Shen, Q.; Wei, H.; Zhou, Y.; Huang, Y.; Yang, H.; Wang, D.; Xu, D. Properties of Amorphous Calcium Carbonate and the Template Action of Vaterite Spheres. *J. Phys. Chem. B* **2006**, *110* (7), 2994–3000.
- (14) Pouget, E. M.; Bomans, P. H. H.; Dey, A.; Frederik, P. M.; de With, G.; Sommerdijk, N. A. J. M. The Development of Morphology and Structure in Hexagonal Vaterite. *J. Am. Chem. Soc.* **2010**, *132* (33), 11560–11565.
- (15) Andreassen, J.-P. Formation Mechanism and Morphology in Precipitation of Vaterite-Nano-Aggregation or Crystal growth? *J. Cryst. Growth* **2005**, *274* (1–2), 256–264.
- (16) Rodriguez-Blanco, J. D.; Shaw, S.; Benning, L. G. How to Make 'Stable' ACC: Protocol and Preliminary Structural Characterization. *Mineral. Mag.* **2008**, *72* (1), 283–286.
- (17) Parkhurst, D. L.; Appelo, C. A. J. *User's Guide to PHREEQC*, version 2, a Computer Program for Speciation, Batch-Reaction, One-Dimensional Transport, and Inverse Geochemical Calculations; U.S. Geological Survey: Denver, CO, 1999; p 312.
- (18) Marchal, J.; Tartoni, N.; Nave, C. Synchrotron Applications of Pixel and Strip Detectors at Diamond Light Source. *Nucl. Instrum. Methods Phys. Res., Sect. A* **2009**, *604* (1–2), 123–126.
- (19) Bateman, J. E.; Derbyshire, G. E.; Diakun, G.; Duxbury, D. M.; Fairclough, J. P. A.; Harvey, I.; Helsby, W. L.; Lipp, J. D.; Marsh, A. S.; Salisbury, J.; Sankar, G.; Spill, E. J.; Stephenson, R.; Terrill, N. J. The HOTWAXS Detector. *Nucl. Instrum. Methods Phys. Res., Sect. A* **2007**, *580* (3), 1526–1535.
- (20) Bruker AXS. TOPAS V4.2, General Profile and Structure Analysis Software for Powder Diffraction Data, User's Manual; Bruker AXS: Karlsruhe, Germany, 2009.
- (21) (a) Hill, R. J.; Howard, C. J. Quantitative Phase Analysis from Neutron Powder Diffraction Data Using the Rietveld Method. *J. Appl. Crystallogr.* **1987**, *20* (6), 467–474. (b) Rietveld, H. M. A Profile Refinement Method for Nuclear and Magnetic Structures. *J. Appl. Crystallogr.* **1969**, *2* (2), 65–71.
- (22) Svergun, D. Determination of the Regularization Parameter in Indirect-Transform Methods Using Perceptual Criteria. *J. Appl. Crystallogr.* **1992**, *25* (4), 495–503.
- (23) (a) de Moor, P.; Beelen, T. P. M.; Komanshek, B. U.; Beck, L. W.; Wagner, P.; Davis, M. E.; van Santen, R. A. Imaging the Assembly Process of the Organic-Mediated Synthesis of a Zeolite. *Chem.—Eur. J.* **1999**, *5* (7), 2083–2088. (b) de Moor, P.; Beelen, T. P. M.; van Santen, R. A. In Situ Observation of Nucleation and Crystal Growth in

Zeolite Synthesis. A Small-Angle X-ray Scattering Investigation on Si-TPA-MFI. *J. Phys. Chem. B* **1999**, *103* (10), 1639–1650.

(24) Benning, L. G.; Waychunas, G. A. Nucleation, Growth, and Aggregation of Mineral Phases: Mechanisms and Kinetic Controls. In *Kinetics of Water-Rock Interactions*; Brantley, S., Kubicki, J., White, A., Eds.; Springer-Verlag: New-York, 2007; pp 259–333.

(25) (a) Teixeira, J. Small-Angle Scattering by Fractal Systems. *J. Appl. Crystallogr.* **1988**, *21*, 781–785. (b) Bale, H. D.; Schmidt, P. W. Small-Angle X-Ray-Scattering Investigation of Submicroscopic Porosity with Fractal Properties. *Phys. Rev. Lett.* **1984**, *53* (6), 596.

(26) Liu, J.; Pancera, S.; Boyko, V.; Shukla, A.; Narayanan, T.; Huber, K. Evaluation of the Particle Growth of Amorphous Calcium Carbonate in Water by Means of the Porod Invariant from SAXS. *Langmuir* **2010**, *26* (22), 17405–17412.

(27) Bolze, J.; Peng, B.; Dingenouts, N.; Panine, P.; Narayanan, T.; Ballauff, M. Formation and Growth of Amorphous Colloidal CaCO<sub>3</sub> Precursor Particles as Detected by Time-Resolved SAXS. *Langmuir* **2002**, *18* (22), 8364–8369.

(28) Laaksonen, A.; Talanquer, V.; Oxtoby, D. W. Nucleation: Measurements, Theory, and Atmospheric Applications. *Annu. Rev. Phys. Chem.* **1995**, *46*, 489–524.

(29) Bolze, J.; Pontoni, D.; Ballauff, M.; Narayanan, T.; Cölfen, H. Time-Resolved SAXS Study of the Effect of a Double Hydrophilic Block-Copolymer on the Formation of CaCO<sub>3</sub> from a Supersaturated Salt Solution. *J. Colloid Interface Sci.* **2004**, *277* (1), 84–94.

(30) Killian, C. E.; Metzler, R. A.; Gong, Y. U. T.; Olson, I. C.; Aizenberg, J.; Politi, Y.; Wilt, F. H.; Scholl, A.; Young, A.; Doran, A.; Kunz, M.; Tamura, N.; Coppersmith, S. N.; Gilbert, P. U. P. A. Mechanism of Calcite Co-Orientation in the Sea Urchin Tooth. *J. Am. Chem. Soc.* **2009**, *131* (51), 18404–18409.

(31) Navrotsky, A. Energetic Clues to Pathways to Biomineralization: Precursors, Clusters, and Nanoparticles. *Proc. Natl. Acad. Sci. U.S.A.* **2004**, *101* (33), 12096–12101.

(32) Gránásky, L.; Pusztai, T.; Tegze, G.; Warren, J. A.; Douglas, J. F. Growth and Form of Spherulites. *Phys. Rev. E* **2005**, *72* (1), 011605.

(33) Keith, H. D.; Padden, F. J. A Phenomenological Theory of Spherulitic Crystallization. *J. Appl. Phys.* **1963**, *34* (8), 2409–2421.

(34) (a) Brečević, L.; Nielsen, A. E. Solubility of Amorphous Calcium Carbonate. *J. Cryst. Growth* **1989**, *98* (3), 504–510. (b) Plummer, L. N.; Busenberg, E. The Solubilities of Calcite, Aragonite and Vaterite in CO<sub>2</sub>–H<sub>2</sub>O Solutions between 0 and 90°C, and an Evaluation of the Aqueous Model for the System CaCO<sub>3</sub>–CO<sub>2</sub>–H<sub>2</sub>O. *Geochim. Cosmochim. Acta* **1982**, *46* (6), 1011–1040.

(35) Pipich, V.; Balz, M.; Wolf, S. E.; Tremel, W.; Schwahn, D. Nucleation and Growth of CaCO<sub>3</sub> Mediated by the Egg-White Protein Ovalbumin: A Time-Resolved in Situ Study Using Small-Angle Neutron Scattering. *J. Am. Chem. Soc.* **2008**, *130* (21), 6879–6892.

(36) Aizenberg, J.; Lambert, G.; Weiner, S.; Addadi, L. Factors Involved in the Formation of Amorphous and Crystalline Calcium Carbonate: A Study of an Ascidian Skeleton. *J. Am. Chem. Soc.* **2001**, *124* (1), 32–39.

(37) Vavouraki, A. I.; Putnis, C. V.; Putnis, A.; Koutsoukos, P. G. An Atomic Force Microscopy Study of the Growth of Calcite in the Presence of Sodium Sulfate. *Chem. Geol.* **2008**, *253* (3–4), 243–251.

(38) Nebel, H.; Neumann, M.; Mayer, C.; Epple, M. On the Structure of Amorphous Calcium Carbonate—A Detailed Study by Solid-State NMR Spectroscopy. *Inorg. Chem.* **2008**, *47* (17), 7874–7879.

(39) (a) Plummer, L. N.; Parkhurst, D. L.; Wigley, T. M. L. Critical Review of the Kinetics of Calcite Dissolution and Precipitation. In *Chemical Modeling in Aqueous Systems*; American Chemical Society: Washington DC, 1979; Vol. 93, pp 537–573. (b) Plummer, L. N.; Wigley, T. M. L.; Parkhurst, D. L. The Kinetics of Calcite Dissolution in CO<sub>2</sub>–Water Systems at 5 to 60 °C and 0.0 to 1.0 atm CO<sub>2</sub>. *Am. J. Sci.* **1978**, *278* (2), 179–216.

(40) (a) Lifshitz, I. M.; Slyozov, V. V. The Kinetics of Precipitation from Supersaturated Solid Solutions. *J. Phys. Chem. Solids* **1961**, *19* (1–2), 35–50. (b) Wagner, C. Theorie der Alterung von

Niederschlägen durch Umlösen (Ostwald-Reifung). *Z. Elektrochem., Ber. Bunsenges. Phys. Chem.* **1961**, *65* (7–8), 581–591.

(41) Butt, H.-J. A Sensitive Method to Measure Changes in the Surface Stress of Solids. *J. Colloid Interface Sci.* **1996**, *180* (1), 251–260.

(42) Lakshmanov, L. Z.; Stipp, S. L. S. Interaction between Dissolved Silica and Calcium Carbonate: 1. Spontaneous Precipitation of Calcium Carbonate in the Presence of Dissolved Silica. *Geochim. Cosmochim. Acta* **2010**, *74* (9), 2655–2664.